Excitation of spin waves in the presence of magnetic charges and monopole polarons in finite-size square artificial spin ice systems

Nimisha Arora [*] and Pintu Das [†]
Department of Physics, Indian Institute of Technology Delhi, Hauz Khas, New Delhi 110016, India

(Received 11 April 2022; revised 21 September 2022; accepted 24 October 2022; published 14 November 2022)

Artificial spin ice (ASI) is a special class of engineered lattice of highly shape anisotropic single domain magnetic nanostructures, which is used as one of the model systems to study the spin ice behavior observed in pyrochlore oxides. The nanomagnets interact via dipolar interaction, resulting in correlated magnetization dynamics exhibiting macroscopic spin configuration states. Here, we exploit the tunability of magnetic microstates in the presence of an external field to study the excitation of spin waves in a finite-size square artificial spin ice system due to a locally applied pulse field. Also, we have studied the excitation in other nanomagnets which are not subjected to the pulse field, which we term as "propagation" of the waves from the perturbed nanomagnets to unperturbed ones purely due to the dipolar coupling. We report that careful selection of vertices with local magnetic charges can effectively direct the anisotropic spin wave excitation in neighboring nanomagnets in the presence of an external field. Further, the investigation has been carried out for spin wave excitation due to the magnetic monopole-polaronic environment forming in closed-edge ASI vertices. Our studies based on micromagnetic simulations suggest that magnetically charged vertices and monopole-polaron formation in square ASI vertices carry spectral signatures such as splitting in higher-frequency bulk mode.

DOI: 10.1103/PhysRevB.106.184411

I. INTRODUCTION

As the conventional electronic charge-transport-based technological devices are approaching the quantum limit, there is a growing thrust on energy-efficient and faster devices based on electron's spin. Recent developments have shown that collective precession of localized magnetic moments (excitation of spin waves) can be used to carry information to a much larger distance in comparison to the conduction electron's spin current. The quantum of spin waves (SWs) is called magnon and the field of studying SWs in magnetic nanostructures has emerged under the name of magnonics [1]. From a classical perspective, SWs can be treated as perturbations in phase-coherent precession of magnetization vectors, which propagate in coupled magnetic media. Due to the very short wavelengths of SWs ($\sim$1 μm to 150 nm depending on the lattice constant of the magnetic material [2]), these are emerging as potential information carriers in energy-efficient miniaturized spin-based devices in the nanoscale regime. Recent studies have reported several SW-based functional device applications in phase shifters [3], microwave antenna [4], directional coupler [5], SW-based multiplexer [6], interferometer [7–9], grating [10], neuromorphic computing [11–14], and memory register [15], etc. Furthermore, it has been reported that phase-incoherent electromagnetic waves can give rise to multiple phase-coherent magnons, which shows the application in energy harnessing and information transfer from alternative sources [16]. Thus, it is clear that the successful implementation of magnonics in modern devices requires the SWs to be controllably guided through nanostructures. Therefore, excitation of SWs of tuned wavelength is one of the major topics of current research in this area [1,17–19]. A fundamental and in-depth understanding of the behavior of SWs in magnetic materials of different nanoscale geometries is essential in order to acquire this ability. In this direction, a particular class of engineered nanostructures, namely, artificial spin ice [20], has stood out as an attractive candidate to study SW behavior in detail. Magnetic nanostructures with high shape anisotropy in artificial spin ice (ASI) geometry exhibit multiple degenerate microstates, which has led to a plethora of studies in the perspective of reconfigurable magnonics [21–37]. The studies suggest that the excitation of SW modes in different nanostructures can be tuned by configuring the underlying magnetization states. In ASI, the SWs have been found to carry information of topological defects, viz., magnetic monopole-antimonopole pair, Dirac string, etc. [38]. Since dipolar interactions play an important role in defining the exact magnetic microstates of ASI systems, these systems are intriguing candidates for studying the interplay of dipolar interaction and SW propagation. Recently, the propagational behavior of SWs has been investigated in unconnected nanostructures with soft magnetic underlayer [26,39] which revealed that SW spectra of ASI display dynamically coupled modes which result in formation of SW nanochannels in the underlayer [26]. Furthermore, nanomagnets exhibiting perpendicular magnetic anisotropy (PMA), arranged in frustrated and unfrustrated geometry with soft magnetic underlayer demonstrate the tunability of nearest-neighbor and next-nearest-neighbor correlations by in-plane perturbation field direction [39]. On the practical front, the

[*] narora1.physics@gmail.com
[†] pdas@physics.iitd.ac.in

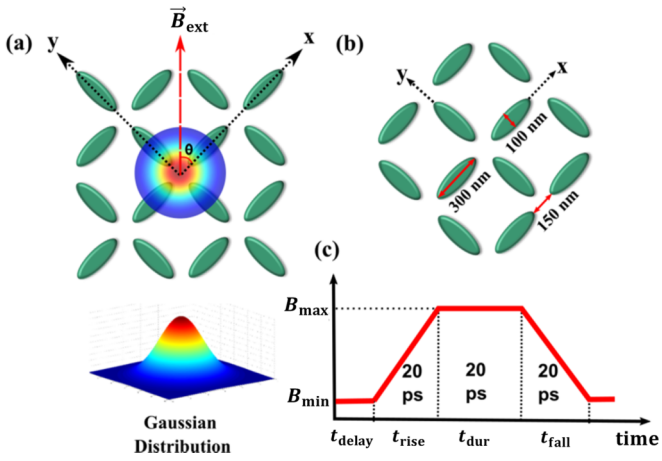

FIG. 1. (a) Schematic diagram of open-edge (OE) sASI system with local transient pulse excitation applied at the center vertex along the z axis (out of the plane) and external bias field applied in the XY plane, making an angle θ with respect to the x axis. The inset below (a) shows the 3D spatial profile of the local excitation, (b) schematic diagram of the closed-edge (CE) sASI, and (c) transient square pulse with rise time (t_{rise}), fall time (t_{fall}), and duration (t_{dur}) of 20 ps each. Nanomagnet dimensions for (a) and (b) here are 300 nm × 100 nm × 30 nm with edge-to-edge interisland gap of 150 nm.

application of SWs in ASI systems was demonstrated in reconfigurable training and reservoir computing via SW fingerprinting [40].

So far, it is not clear how a SW excited in a vertex of an ASI system transmits or propagates to purely dipolar coupled, i.e., unconnected neighboring nanomagnets. Moreover, although specific SW modes have been found to be related to emergent monopole-antimonopole pairs [38], so far, there is no precise analysis of the propagational or transmission behavior of SWs in the presence of magnetic charges in the ASI vertices.

In this work, the role of dipolar interaction in the behavior of SW modes is investigated by performing a detailed micromagnetic analysis of the modes excited by a locally applied pulse field in square ASI (sASI) vertices (Fig. 1). In addition to analyzing the excitation of modes and the power in the nanomagnets at the central vertex where pulse field is applied, we also study in detail how dipolar coupling assists these modes to be excited in the neighboring nanomagnets at the outer vertices which are not subjected to the pulse field. This is discussed in terms of transmission ("propagation") of SW modes in the present context. In order to carry out such a detailed investigation, a finite-size sASI system is used in this work. We observe excitation of localized modes as well as modes excited/propagating up to the next-nearest neighbors where no pulse field is applied. We have also analyzed in detail the behavior of SW modes in the presence of sASI vertices that are magnetically charged. Further analysis of SW modes has been carried out for finite-size sASI vertices with mixed (even- and odd-) coordination numbers. This investigation is motivated by the observation of screened magnetic charges at even-coordinated vertices by the surrounding uncompensated charges at the odd-coordinated vertices, leading to magnetic monopole-polaronic behavior in ASI systems with mixed coordination geometry [41–45]. So far, the behavior of SWs in case of magnetic monopole-polaronic bound state remains unknown. In our simulated structures, the open-edge (OE) sASI corresponds to even coordination, whereas closed-edge (CE) sASI (shown in Fig. 1) corresponds to mixed coordination vertices. We note here that a detailed investigation of the SW behavior, as discussed above, requires finite-size systems, particularly since true propagation in such unconnected nanostructures is not significant.

II. METHOD

For the investigations, we carried out detailed micromagnetic simulations for the sASI structures (see Fig. 1) using finite-difference discretization based (open-source) GPU-accelerated software MUMAX3 [46]. Here, the evolution of space- and time-dependent magnetization vector, $\vec{m}(\vec{r}, t)$, is calculated at each cell of the discretized geometry by employing the Landau-Lifshitz-Gilbert equation [Eq. (1)]:

$$\vec{\tau}_{LL} = \frac{\partial \vec{m}}{\partial t} = \gamma_{LL} \frac{1}{1+\alpha^2} [\vec{m} \times \vec{B}_{eff} + \alpha[\vec{m} \times (\vec{m} \times \vec{B}_{eff})]] \tag{1}$$

with τ_{LL} is the Landau-Lifshitz torque, $\vec{m}(\vec{r}, t)$ is the reduced magnetization vector of unit length, γ_{LL} is the gyromagnetic ratio (rad/Ts), α is the dimensionless damping parameter, and $\vec{B}_{eff}$ is the effective magnetic field.

Here, $\vec{B}_{eff} = \vec{B}_{ext} + \vec{B}_{demag} + \vec{B}_{exch} + \vec{B}_{anis} + \vec{B}_{exc}(t) + \cdots$ with $\vec{B}_{ext}$, $\vec{B}_{demag}$, $\vec{B}_{exch}$, $\vec{B}_{anis}$, and $\vec{B}_{exc}(t)$ are the external bias field, demagnetization field, exchange field, anisotropy field, and time-varying excitation (magnetic) field, respectively. For the micromagnetic simulations, the nanomagnetic structures of $Ni_{80}Fe_{20}$, as shown in the schematic diagram [Figs. 1(a) and 1(b)], are discretized in cuboidal cells of 5 nm length, which is less than the exchange length (5.3 nm) of $Ni_{80}Fe_{20}$. Experimentally reported value of saturation magnetization $M_{sat} = 8.6 \times 10^5$ A/m, exchange stiffness constant $A_{ex} = 1.3 \times 10^{-11}$ J/m, and damping coefficient $\alpha = 0.5$ for $Ni_{80}Fe_{20}$ are used throughout the study [47]. In order to determine the SW behavior, a reduced damping coefficient of 0.008 is used. This enables a prolonged precession of weak modes, thereby allowing for a detailed analysis of such modes [48].

SWs are excited by perturbing the equilibrium macrospin state corresponding to a static in-plane bias field ($\vec{B}_{ext}$) via an out-of-plane temporal field pulse (see Fig. 1). The equilibrium (macro) spins configuration is first evaluated by quasistatically down-sweeping the external in-plane bias field from 250 mT to $\vec{B}_{ext}$ and performing energy minimization using the fourth-order Runge-Kutta method. At this state, a transient square pulse field of amplitude $B_{max} = 3$ mT with rise time t_{rise}, fall time t_{fall}, and pulse duration t_{dur} of 20 ps each is applied along the z direction (out of plane). The transient excitation field pulse is convoluted with Gaussian function in space to locally excite the central vertex region of the OE geometry [see Fig. 1(a)]. After the incidence of the pulse, time evolution of reduced magnetization vector [$\vec{m}(t)$] is recorded for 4 ns at time step (Δt) of 10 s. To extract the frequencies of the excited SW modes, a fast Fourier transformation (FFT) is performed on the recorded $\vec{m}(t)$ data. Thus, power spectra for SW modes are determined for a given magnetic structure.

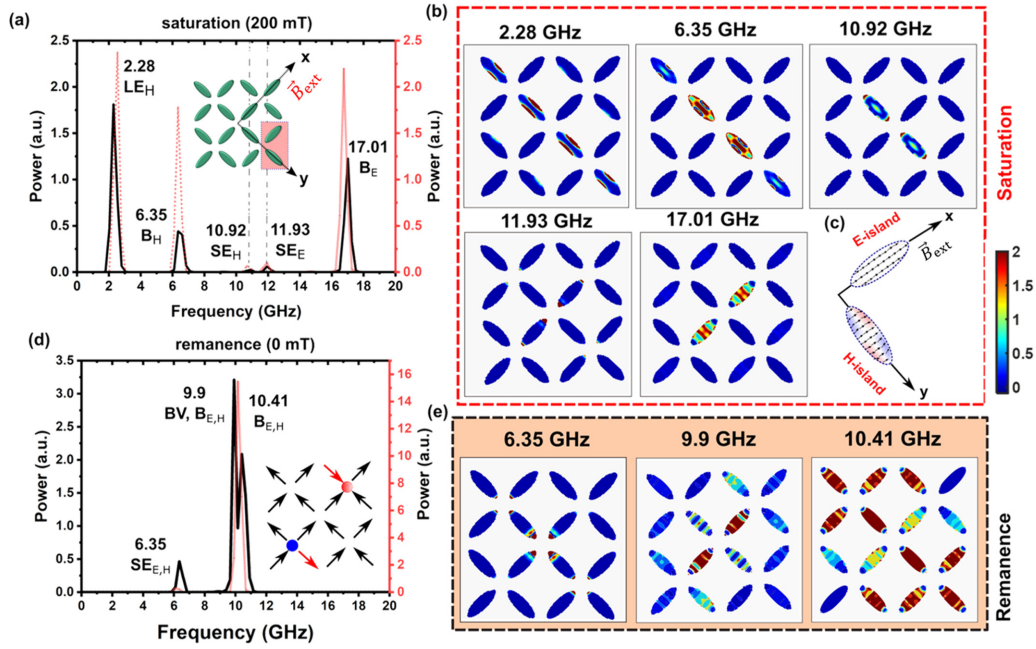

FIG. 2. SW spectra (black solid line) for open-edge vertex at saturation, i.e., $\vec{B}_{\text{ext}} = 200$ mT applied along x axis (a) and at remanence (d). Spectra for individual nanomagnets for bias field of 200 mT applied along the easy axes (E islands, red solid line) and the hard axes [H islands, red dotted line, shown in (a)] and at remanence shown using red solid line in (d). Inset in (a) shows the schematic diagram for applied field direction, and that in (d) shows the schematics of macrospin configurations at remanence, (c) micromagnetic simulation results for internal spin configuration in the perpendicularly placed islands for $\vec{B}_{\text{ext}} = 200$ mT as highlighted in the inset of (a). The power profile of the excited SW modes for open-edge vertex at saturation (b) and remanence (e). The color bar shows the FFT power of real-time fluctuations of the z component of magnetization in an arbitrary unit.

The nature and the origin of the SW modes are analyzed by investigating the power and phase profiles of the excited SW modes at particular frequencies using MATLAB code (see Supplemental Material [49]). The role of dipolar interaction in the excitation of SW modes in neighboring nanomagnets is quantified by comparing the power of SW modes in perturbed central vertex and unperturbed outer vertex in two orthogonal directions. This study was performed at two external field configurations, viz., saturation and remanence for both even- and mixed-coordinated vertices. Additionally, to obtain a clear insight into the role of magnetic charges and monopole-polaronic environment on the SW mode behavior, a transient square pulse field is uniformly applied along the z direction on all nanomagnets in CE and OE vertex geometries. SW analysis is then performed in the range of ± 150 mT of $\vec{B}_{\text{ext}}$, where $\vec{B}_{\text{ext}}$ is applied along one of the easy axes of the magnetic sublattice.

III. RESULTS AND DISCUSSION

Figure 2 shows the SW spectra for OE vertex geometry (vertices with even coordination) for saturated state corresponding to the bias field of $\vec{B}_{\text{ext,x}} = 200$ mT as well as remanent state, i.e., $\vec{B}_{\text{ext,x}} = 0$ mT, where $\vec{B}_{\text{ext,x}}$ denotes the field applied along the x direction as clarified in Fig. 2(c). At saturation, the spectrum exhibits five peaks corresponding to the five different modes of excitations of SWs in the frequency range of 2–17 GHz [see Fig. 2(a)]. In the studied system involving 16 nanomagnets, the applied field direction is along easy axes and hard axes of 8 nanomagnets each [see Fig. 2(a) inset] henceforth identified as E islands and H islands, respectively [see Fig. 2(c)]. As the orientation of the external bias field applied in this case corresponds to easy as well as hard directions of different nanomagnets, we have analyzed SW behavior of *individual* islands with external field along both easy and hard directions. This allows us to carry out an in-depth analysis of the role of individual nanomagnets in the overall SW spectra of the dipolar coupled system. The results are shown in Fig. 2(a). A comparison of the SW modes excited in the individual nanomagnets with that of the coupled sASI system [Fig. 2(a)] shows that although the modes associated with coupled system display a nominal frequency shift of up to ∼0.3 GHz which accounts for the stray field of ∼3.6 mT, yet it consists of all the modes excited in individual E as well as H islands. The shift may be a result of the influence of an additional dipolar field emanating from the interacting nanomagnets. Thus, these results suggest that as the spins are strongly pinned along the direction of the $\vec{B}_{\text{ext}}$ at the saturated state, the SW modes in individual nanomagnets remain largely unaffected in the dipolar coupled sASI system.

In order to determine the origin of these peaks in the observed power spectra, we analyze the power profiles of the excited SW modes corresponding to each of the five frequencies where a peak is observed. The power profiles are shown in Fig. 2(b). We make the following four interesting observations: (i) significant mode power for the three lower-frequency modes, viz., 2.3, 6.4, and 10.9 GHz, appears to be concentrated primarily in the H islands. This indicates that the peaks observed at those frequencies are primarily due to modes excited in the H islands. (ii) With increasing

frequencies, inhomogeneously distributed power is systematically reduced in the H islands. For the SW mode at 2.3 GHz, the excited mode exhibits significant power in the four H islands, whereas, for SW mode at 10.9 GHz, the power is found to be mainly concentrated in the two H islands coupled to the central vertex. (iii) Two higher-frequency modes appearing at 11.9 and 17 GHz are primarily excited at the E islands. Large power corresponding to these modes is primarily located at the E islands of the central vertex. (iv) The excited SW modes in both E and H islands are inhomogeneously distributed. In general, the demagnetization field in confined magnetic nanostructures may be inhomogeneous, resulting in multiple low-energy potential wells where spins are in local equilibrium corresponding to the internal local field. Curling of magnetization observed near the edges of H islands is an example of one such inhomogeneity of demagnetization field [see Fig. 2(c)]. Such inhomogeneous demagnetizing field within the individual sASI nanostructures may, in turn, lead to inhomogeneously distributed local excitation of SWs in the sASI structures. According to the spatial distribution of the modes, we identify the modes observed at the edges of nanomagnets as edge modes and the others excited within the "bulk" of the nanomagnets as bulk modes (hereafter B mode). Thus, we identify the 2.3-GHz mode as long-edge (LE_H) mode and 11.9 GHz as short-edge (SE_E) mode. The subscripts denote the H and E islands, respectively.

From the power distribution profile at saturation, we also observe that the lower-frequency LE_H mode appears to extend to the nearest-neighbor H islands restricted along the direction perpendicular to that of $\vec{B}_{ext}$. The demagnetization field for H islands is larger than that for the E islands, thereby reducing the effective in-plane field ($\vec{B}_{eff}$) in H islands compared to that for E islands. The total field $\vec{B}_{tot}[= \vec{B}_{eff} + \vec{B}_{exc}(t)]$ during temporal pulse excitation along the z direction thus makes a larger angle with respect to the in-plane direction of $\vec{B}_{eff}$ resulting in larger fluctuations in z component of magnetization in H islands. Since $f \propto B_{tot}$, therefore, the perturbation in phase-coherent precession, which manifests itself as a SW, has a higher probability of transmission ("propagation") to the nearest neighbor of H islands which in this case, along the y axis for lower-frequency mode ~2.3 and 6.4 GHz. Along the x axis, adjacent H islands are separated by a much larger distance ~450 nm. At this separation, the resulting stray field variation due to fluctuations in z magnetization is negligible. Thus, we do not observe transmission of SW mode along field direction or x axis.

At remanence ($\vec{B}_{ext} = 0$), the magnetization in each nanomagnet orients along their easy directions. Due to the magnetostatic interactions, low-energy 2-in/2-out spin ice states are observed for three vertices, whereas the remaining two vertices exhibit magnetically charged excited states [see inset of Fig. 2(d) for a schematic diagram]. The magnetic charges are reconciled considering the nanomagnets as a dumbbell of two equal and opposite magnetic charges (dumbbell model) [50]. For this magnetic configuration of the sASI system at remanence, the number of SW modes is now reduced to three from five compared to the saturated state. In this case, both E and H islands are now identical with respect to an external transient field perturbation which accounts for the observed fewer numbers of peaks in remanence. The peaks

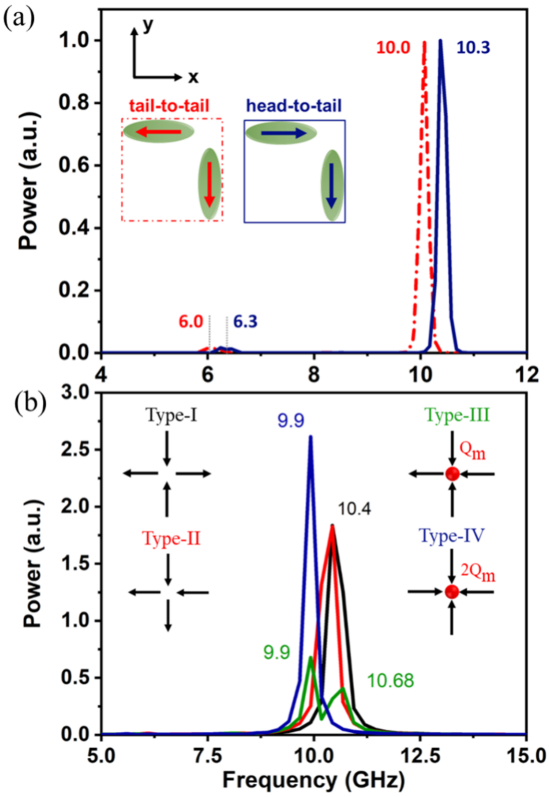

FIG. 3. (a) SW spectra of L-shaped geometry at remanence in two magnetic state configurations, viz., tail to tail (magnetically charged vertex) and head to tail (magnetically uncharged vertex). Inset shows the magnetic states (tail-to-tail as well as head-to-tail configuration) of the nanomagnets in L-shaped geometry. (b) SW spectra of single vertex geometry with predefined magnetization configurations, viz., types I, II, III, and IV. Inset shows the arrow diagram of investigated macrospin's configuration.

in the SW spectra are observed at the frequencies of 6.4, 9.9, and 10.4 GHz, respectively, as shown in Fig. 2(d). To clearly analyze the role of dipolar interactions in the SW spectra in this case, we have calculated the SW modes for *individual (i.e., noninteracting)* nanomagnets with magnetization along the easy directions. The simulation results show that only two SW modes, viz., 6.4 and 10.4 GHz, are excited in an individual nanomagnet of the same dimensions, thereby indicating a possible role of dipolar interactions on the excitation of 9.9-GHz mode in such dipolar coupled nanostructures. Therefore, to elucidate the origin of this 9.9-GHz mode, we analyze a fundamental cell consisting of two dipolar-coupled nearest-neighbor nanomagnets: one E and one H island in L-shaped geometry [see Fig. 3(a)]. The SW spectra of the L-shaped geometry at remanence, where the magnetization in the islands orients as a head-to-tail configuration resulting in zero magnetic charge at the meeting point (junction) of the nanomagnets, exhibit two peaks at the frequencies of 6.3 and 10.3 GHz, respectively. Since the individual nanomagnets show similar SW behavior, these observations suggest that such head-to-tail (i.e., zero magnetic charge) configuration in L-shape geometry retains the SW behavior of individual nanomagnets. However, as the magnetization of the L-shaped geometry is predefined as head-to-head or tail-to-tail

configurations leading to a magnetic charge at the junction, the SW spectra show a redshift of ∼0.3 GHz with respect to that observed for individual nanomagnets, thereby exhibiting a strong mode at 10 GHz as shown in Fig. 3(a). This demonstrates a clear role of magnetic charges due to dipolarly interacting nanomagnets on the excitation of SWs. This 10-GHz mode appears to be excited at 9.9 GHz in the sASI system with mixed types of charged and chargeless vertices. This suggests that SW spectra for vertices with mixed charge state may exhibit SW modes as observed in Fig. 2(d). In order to confirm the specific SW modes due to dipolarly coupled charged vertices, we investigated the spectra due to individual vertices of four different types, viz., type I to type IV [see Fig. 3(b)], where types III and IV have magnetic charges Q_m and $2Q_m$, respectively (see discussions on dumbbell model). Type I and II vertices are the uncharged vertices where only a single SW mode at 10.4 GHz is excited. Interestingly, this mode at the charged type III vertex appears to be split into two modes of frequencies 9.9 and 10.7 GHz, whereas the other charged type IV vertex exhibits only one mode at 9.9 GHz [see Fig. 3(b)]. Such splitting of modes due to charged vertices was earlier reported by Gliga *et al.* [38]. However, there the observed mode splitting in the array of vertices comprising 112 nanomagnets was suggested to be due to the slightly different frequencies of oscillations of charged vertices located at the boundary and interior of the array (for edge modes) or due to the presence of Dirac string (for bulk ferromagnetic resonance mode). Our studies of individual vertices clearly show that the mode at 9.9 GHz appears due to the formation of magnetic charge at individual vertices. Thus, these results for individual vertices underline the fact that the magnetostatic interaction between nanomagnets leading to 3-in/1-out or 3-out/1-in type locally charged vertices modifies the local magnetic structure of the involved nanomagnets in such a way that an additional SW mode is excited in these nanostructures. We identify this 9.9-GHz mode as charged vertex (CV) mode in the following.

It is clear that the dipolar interaction plays a significant role in exciting the CV mode in the vertex. In order to identify the critical separation (lattice constant) between the nanomagnets above which the mode vanishes, we investigate the SW modes of the OE vertex system with varying interisland separations. The spectral behavior was investigated by varying the edge-edge separation of the colinear nanomagnets from 100 nm to 1 μm. We observe that although the static magnetic behavior (i.e., macrospin configuration) of the sASI system remains unaltered in the entire range of separation (i.e., 100 nm–1 μm), the excitation of the CV mode at 9.9 GHz is observed until the separation of ∼225 nm (see Supplemental Material for details [49]). Beyond 225 nm, only the two modes, as observed for individual nanomagnets, are observed. Based on these observations, we identify the separation up to 225 nm as the strongly interacting regime for collective SW excitation.

Next, to investigate the nature of the excited SW modes at remanence in detail, the power profiles of the modes are calculated. As shown in Fig. 2(e), excitations for the three frequencies are observed in both types of nanomagnets. However, the modes can be distinctly identified according to the distribution of the power profiles within the individual nanomagnets. The excitation of 6.4 GHz mode appears to be

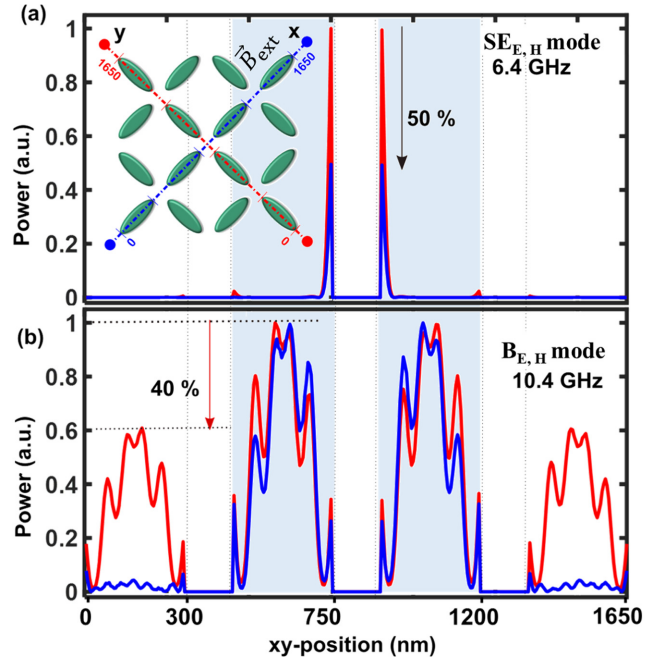

FIG. 4. Line power profile for the excited SW mode at (a) 6.4 GHz and (b) 10.4 GHz in the remanent state, along the two orthogonal directions as shown in the inset of (a) (blue: along x, red: along y). Highlighted regions correspond to nanomagnets at the central vertex, which are under pulse-field excitation.

localized near the short edges (SE mode), whereas the 9.9- and 10.4-GHz modes are excited in the bulk of the nanomagnets.

The SE 6.4-GHz mode exhibits more substantial power along the direction perpendicular to the bias field than along the field direction. This is exemplified by plotting the line profile of the power map [Fig. 2(e)] along the x and y directions through the central vertex, as shown in Fig. 4. The line profile clearly indicates that the power of the 6.4-GHz mode excited at the central vertex nanomagnets along the x direction is reduced by almost 50% compared to that along the y direction. The nominal power of ∼2% at the other end of these nanomagnets is observed only along the y direction. No power for excitation is observed in the nanomagnets of outer vertices. Thus, we find that the excited SE mode is strongly localized at the central vertex where the pulse field is applied. For the bulk SW mode of ∼10.4 GHz, the observed power of excitation at the two nanomagnets involved at the central vertex is nearly the same for both E and H islands. However, for nanomagnets involved at the outer vertices, the observed power along the y axis is nearly 60% of the maximum power observed at the central vertex [see Fig. 4(b)]. In contrast, a nominal power of only ∼2% of the maximum power is observed at the nanomagnets of the outer vertices along the field direction. This may indicate a SW "propagation" of the bulk 10.4-GHz mode to the dipolarly coupled next-nearest-neighbor nanomagnets along the direction perpendicular to the initial applied bias field direction. The weak "propagation" in this case can be explained by the SW dispersion calculated for these unconnected nanostructures (not shown). The power profile for the CV mode observed at 9.9 GHz is significantly different from the other two modes. Here, the power is found

to be concentrated mainly at the nanomagnets involved at the central vertex and the nanomagnets with magnetization along the y direction at the outer vertices with nonzero local charges [see Fig. 2(e) and inset of Fig. 2(d)]. The power profile of this mode in the H islands of the central vertex exhibits nodal lines perpendicular to the magnetization orientation. This profile is characteristic of backward volumelike mode (BV). However, the power of the mode is distributed in the bulk of the rest of the nanomagnets. Thus, the 9.9-GHz mode can be identified as hybridized BV and B mode. Furthermore, the power profile of the mode is also found to be asymmetrically distributed in nanomagnets [see Fig. 2(e)]. Since the E islands at the central vertex are directly coupled with the charged vertex and are under the direct transient pulse excitation, therefore, significant power of the CV mode is observed in these nanomagnets. On the other hand, the H islands at the central vertex are under direct pulse excitation but not directly coupled with the noncentral charged vertex. These H islands, however, exhibit a resonant mode at 10.4 GHz, which is close to the CV mode and thus exhibits hybridization. This may give rise to the observed asymmetric power distribution in the power profile of the CV mode.

The above analyses suggest that the SW modes (SE and B modes) in such unconnected highly shape anisotropic nanomagnets in sASI geometry show preferential excitation in the neighboring nanomagnets positioned along the direction perpendicular to the external bias field direction. We note here that this is also the direction along which the two charged vertices are present in the system at the ground state. Thus, so far, it is not clear if the "propagation" direction is affected by the external field or the presence of magnetic charges. In order to elucidate this further, we investigated the SW behavior of the sASI system as a function of applied field direction. By applying an external bias field along different directions, the remanent magnetic states of the individual nanomagnets are tuned. The SW modes for these investigations are calculated for $\theta = 45°$, $90°$, and $135°$, respectively, where θ is the angle between the applied field direction and x axis [see Fig. 1(a)]. For $\theta = 45°$, the magnetic configuration of the sASI system at remanence exhibits chargeless 2-in/2-out vertices in the sASI system as shown in Fig. 5(a). The SW spectra for this chargeless sASI state exhibit only two excited modes at 6.4 GHz (SE mode) and 10.4 GHz (B mode), respectively. Interestingly, excitation of only these two modes was earlier observed for individual nanomagnets and chargeless L-shaped geometry, as discussed above. Here we observe a remarkable difference in the power profile of a 6.4-GHz mode calculated for the magnetic configuration corresponding to $\theta = 45°$ in comparison to that observed for $\theta = 0°$. As shown in Figs. 5(b) and 5(d), the SE mode for this magnetic configuration is found to be excited in all the nanomagnets, whereas for $\theta = 0°$ the mode power at the two farthest nanomagnets along the x axis is nearly zero suggesting no excitation of the SW mode in those islands. For this chargeless state at $\theta = 45°$, the sASI system is magnetically symmetric with respect to the applied bias field. Therefore, the SE mode is excited symmetrically in all the nanomagnets. However, for $\theta = 0°$, the sASI system is magnetically asymmetric with respect to the bias field. Under this condition, magnetically charged sASI vertices are generated, as discussed above. Our analysis suggests that these

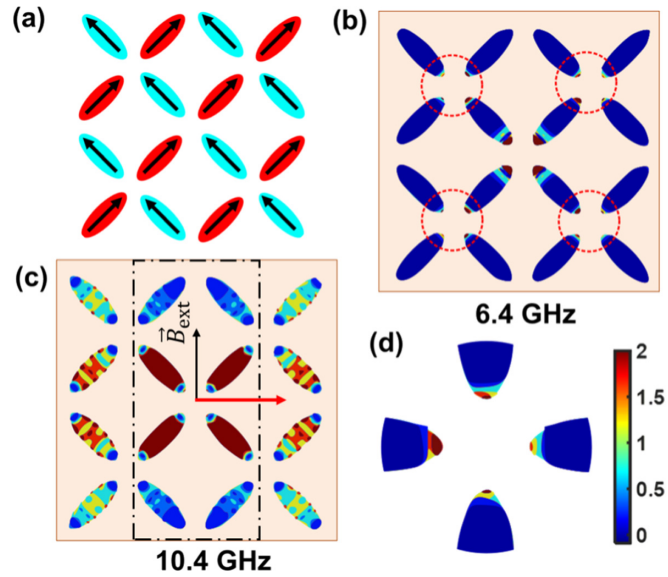

FIG. 5. (a) Equilibrium magnetization state for OE vertex at remanence with $\theta = 45°$. The power profile of the SE mode excited at 6.4 GHz (b) and B mode excited at 10.4 GHz (c) in remanence with $\theta = 45°$. Here $\vec{B}_{ext}$ denotes the direction of an external field that is applied before reaching the remanent state and a red arrow shows its corresponding orthogonal direction. A black dashed-dotted rectangular box encloses the nanomagnets positioned along the external bias field orientation. (d) The zoomed power profile of the vertex region as highlighted with a red dotted circle in (b). The color bar shows the FFT power of real-time fluctuations of the z component of magnetization in an arbitrary unit.

charged vertices for $\theta = 0°$ are responsible for the observed asymmetric *excitation* of the SE mode *in the neighboring nanomagnets*. For 10.4-GHz B mode, we observe that unlike for the case of $\theta = 0°$, here all the four nanomagnets at the central vertex are symmetrically excited [see Fig. 5(c)]. Moreover, the power of the mode in outer nanomagnets appears to depend on the direction of the external field applied initially before reaching the remanent state. Nanomagnets towards the field direction [shown by a black arrow in Fig. 5(c)] apparently exhibit less power compared to the ones perpendicular to the field direction [shown by a red arrow in Fig. 5(c)]. For $\theta = 0°$, earlier we observed that the 10.4-GHz mode has higher power in the nanomagnets which are oriented along the direction perpendicular to the bias field orientation. This suggests that the orientation of the external bias field predefines the magnetic state in such a way that an asymmetric excitation (propagation) of the mode occurs in the outer nanomagnets. We note here that the CV mode is absent in the SW spectra for $\theta = 45°$ where all the vertices are magnetically uncharged. Our additional calculations performed for $\theta = 135°$ show a similar behavior of the SW modes as for $\theta = 45°$. For $\theta = 90°$, i.e., when the bias field is applied along the y direction (see Supplemental Material, Fig. S3a [49]), the remanent state exhibits two charged (outer) vertices positioned along the field direction. Thus, these charged vertices for $\theta = 90°$ appear in a direction orthogonal to the charged vertices observed for $\theta = 0°$ case. Interestingly, the SW spectra for this case again show the CV mode in addition to the SE and B modes (see

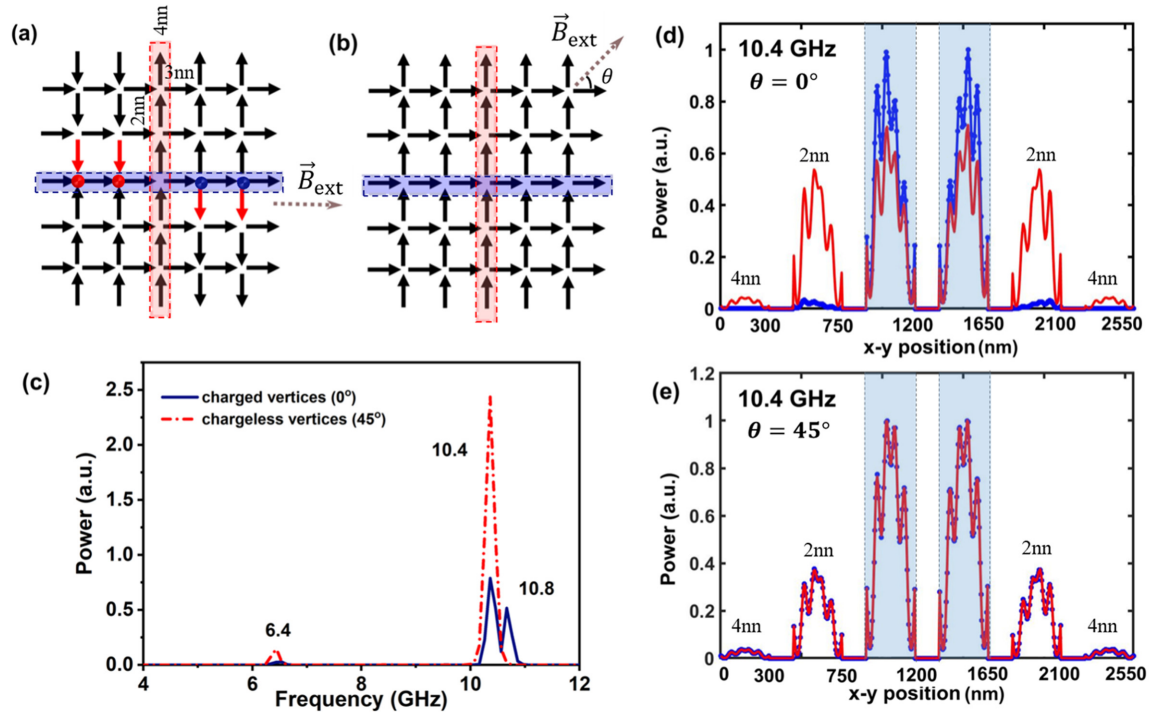

FIG. 6. Equilibrium macrospin configuration in sASI array at remanence when initial bias field applied along one of the easy axes, i.e., 0° (a) and at 45° (b) with respect to the easy axis of one of the sublattices. Red and blue dots at the outer vertices present along the central horizontal axis (highlighted in the blue box) denote the presence of charged vertices with type III macrospin configuration. Red and blue color notations in these field circles are adopted for the net local diverging flux Q_m and converging flux $-Q_m$, respectively. (c) SW spectra for 5×5 vertex array for equilibrium state shown in (a) and (b). The line power profile of the bulk SW mode excited in the sASI array at remanence across the two orthogonal directions [highlighted region shown in (a) and (b)] when the initial bias field is oriented along one of the easy axes, i.e., 0° (d) and at 45° (e) from the easy axis of one of the sublattices. Red and blue lines denote the line power profile across the horizontal and vertical direction [a blue and red highlighted region in (a) and (b)], respectively. Highlighted regions in (d) and (e) correspond to central vertex nanomagnets under field pulse excitation.

Fig. S3b in the Supplemental Material [49]). These results clearly demonstrate the following three facts: one, although the pulse field is applied at the four nanomagnets of the central vertex [Fig. 1(a)], specific SW excitations are observed in other nanomagnets involved at the outer noncentral vertices. This suggests a transmission or propagation of excited SWs to the next-nearest neighbors. Thus, it appears that the dipolar coupling of the nanomagnets facilitates carrying the specific information of SWs from one nanomagnet to another, however, with reduced intensity. The "propagation" or "transmission" is limited to the next-nearest neighbor. Second, the presence of "sources" and "sinks" of magnetic flux favors excitation of a specific CV mode, 9.9 GHz for the given structure. Third, the excitation of B mode at 10.4 GHz in specific noncentral nanomagnets, which is termed as SW transmission or propagation in the present context, appears to depend on the orientation of the bias field. Also, we observe that the *transmission* of SE mode to the neighboring (next-nearest-neighbor) nanomagnets is impeded by the "source" or "sink" of magnetic flux [see Fig. 2(e)]. Thus, our results show that by tuning charged magnetic state in such structures, guided or directional SW "propagation" to neighboring nanomagnets can be realized due to magnetostatic interaction between such unconnected nanostructures.

Although it is clear that the SW "propagation" in such unconnected nanostructures is limited to the neighboring nanomagnets only, however, the exact distance up to which SW propagates is not clear. In order to investigate this, we have calculated the behavior of SWs for a larger array of vertices. An array of 5×5 vertices at a remanent state with two different initial bias field configurations, viz., with field along the horizontal direction and along 45° with respect to the horizontal direction, is considered for the analysis. For $\vec{B}_{ext}$ applied along the horizontal direction (one of the easy axes of the nanomagnets), the magnetic configuration at the remanent state exhibits two pairs of charged vertices (i.e., two "sources" and two "sinks" of flux) separated by an uncharged 2-in/2-out type vertex along the external field direction as schematically depicted in Fig. 6(a). Thus, we observe similar magnetic behavior as for the 5-vertex case discussed above, except that in this case of an array of 25 vertices, two pairs of charged vertices instead of one pair are observed. We note that here one pair is excited at the interior of the array and the other pair at the two edges of the array. We next investigate the SW excitation in all the nanomagnets again by applying a square pulse field, with Gaussian spatial distribution of similar specification as before, at the central uncharged vertex [see Fig. 6(a)] and calculate the SW spectra for the entire system. Here again, for $\theta = 0°$ the calculated SW spectra exhibit three excited modes, however, at frequencies of 6.4 GHz (SE mode), 10.4 GHz (B mode), and 10.8 GHz (B mode) as shown in Fig. 6(c). The power profiles are shown in the Supplemental

Material in Fig. S4. The presence of charged vertices at the interior and the edges, in this case, may lead to the excitation of the two B modes at slightly different frequencies in comparison to the 5-vertex case described above. For $\theta = 45^\circ$ where vertices are chargeless, only two modes, viz., at 6.4 and 10.4 GHz, are excited. These modes correspond to the SE and B modes (see Supplemental Material Fig. S4 for power profiles [49]).

In order to obtain quantitative information about the distance up to which the SW modes are observed in the unperturbed nanomagnets surrounding the perturbed central vertex, we investigate the power profiles (see Supplemental Material, Fig. S4 [49]) of the modes across the two orthogonal directions highlighted in Figs. 6(a) and 6(b). From the line profile of power of 10.4-GHz B mode for $\theta = 0^\circ$ (array with charged vertices), we observe a significant SW power appearing in the next-nearest neighbor that lies along the y direction [see Fig. 6(d)]. The "propagation" in this case is asymmetric as there is strongly reduced excitation along the direction in which charged vertices are located.

However, for $\theta = 45^\circ$, SWs appear to "propagate" symmetrically in both the x and y directions [see Fig. 6(e)] owing to the geometrical symmetry of the system with respect to the applied bias field. The results are consistent with the observations made for the 5-vertex case discussed above. To quantify the transmission to the unperturbed nanomagnets, we calculate the transmission coefficient $(\frac{P_{\text{neighbor-island}}}{P_{\text{center-island}}})$ in both the aforementioned cases where $P_{\text{center-island}}$ and $P_{\text{neighbhor-island}}$ are corresponding powers at central and a neighboring island, respectively. For $\theta = 0^\circ$, we observe that the B mode shows efficient transmission to the next-nearest-neighbor (2NN) vertices with transmission coefficient ~0.75 towards the direction perpendicular to the initial bias field, which reduces to 0.07 at the 4NN nearest neighbor [see Fig. 6(a)]. However, along the direction of charged vertices, a transmission coefficient of only ~0.02 is observed at the next-nearest neighbor (2NN). For $\theta = 45^\circ$ with no charged vertices, symmetric transmission along both the orthogonal directions with a transmission coefficient of ~0.4 at the next-nearest neighbor (2NN) [see Fig. 6(e)] is observed.

In large arrays of such sASI systems, structures are often fabricated so that additional islands are patterned at the edges, thus forming CE systems; see Fig. 1(b) for a schematic diagram. To complete our understanding of SWs in these sASI systems, we next investigate the SW excitation in CE vertex and compare the results with that for the OE vertex. For this study, field pulse is *uniformly applied* to the entire vertex system for both OE and CE vertices. We note here that unlike for OE vertices as discussed above, the CE vertices are of mixed coordination. The vertices at the edges are of coordination No. 3 and that at the center is of No. 4 [see Fig. 1(b)] results in an uncompensated magnetic charge at the odd-coordinated 1-in/2-out or 2-in/1-out type vertices. Our earlier work [51] shows that for such mixed-coordinated vertices, the net distribution of charges at outer vertices screen and compensate any charge that is formed at inner or central even-coordinated vertex. The cloud of charges at the border then forms magnetic monopole polarons [44,45,51] which is otherwise absent in the case of OE vertices. The behavior of

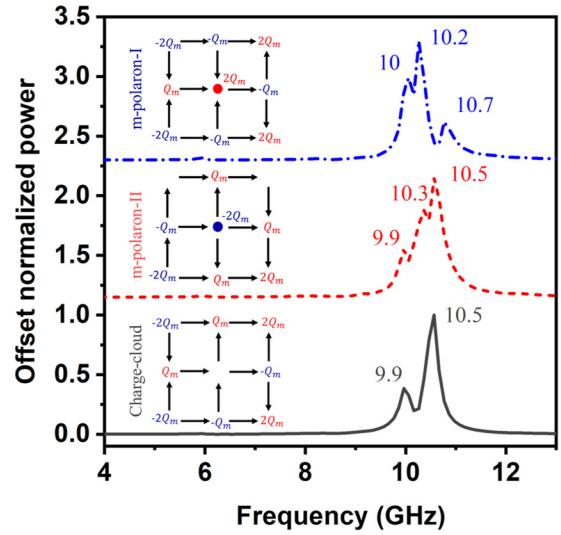

FIG. 7. SW spectra for CE vertex with predefined macrospin configuration resulting in the polaronic and nonpolaronic environment. Insets show the arrow diagrams of the studied polaronic case with two different configurations of uncompensated charges with a central charged vertex state and a nonpolaronic case with only a charge cloud present due to uncompensated charges at the edges.

SWs in a monopole-polaronic environment is an open question that we address here.

Accordingly, we investigate the feasibility of forming a magnetic monopole-polaron in the presence of an external field and study its influence on SW dynamics. Our simulation results for the CE vertex show that in the investigated field range of ±150 mT, CE vertex exhibits zero magnetic charge at the center vertex. The magnetic charge cloud comprising of uncompensated $\pm Q_m$ charges at the border (see inset of Fig. 7) is distributed such that the net magnetic charge of the CE-vertex system remains zero. The SW spectrum for this magnetic state at remanence shows two SW modes at 10.1 and 10.6 GHz, respectively. However, the spectrum for OE vertices under uniform excitation at remanence shows three SW modes at 6.4, 10.3, and 10.6 GHz. This suggests that the weak mode of 6.4 GHz excited in OE vertex diminishes to negligible power in CE vertex with charge cloud and 10.3-GHz mode is redshifted to 10.1 GHz. This observation is consistent with our earlier analysis showing the redshift of SW modes by ~0.3 GHz in a charged vertex state. Thus, this redshift, in this case, may also be accounted for the charge cloud in CE vertex. Details of the mode profiles are given in the Supplemental Material (see Fig. S5) [49]. In the CE vertex discussed above, energy minimized ground state does not result in a monopole polaron since the central vertex is found to be of zero magnetic charge. We, therefore, used a predefined monopole polaron system to analyze the SWs in the monopole-polaronic environment. Two different configurations of macrospins forming monopole polarons, viz., polaron I and polaron II, as typically observed in experiments, are considered [41] (see insets of Fig. 7). For both the monopole-polaronic states, three modes are excited. For polaron I, SW modes appear at 10, 10.2, and 10.7 GHz whereas for polaron II, SW modes appear at 9.9, 10.3, and 10.6 GHz, respectively. For comparison, we also

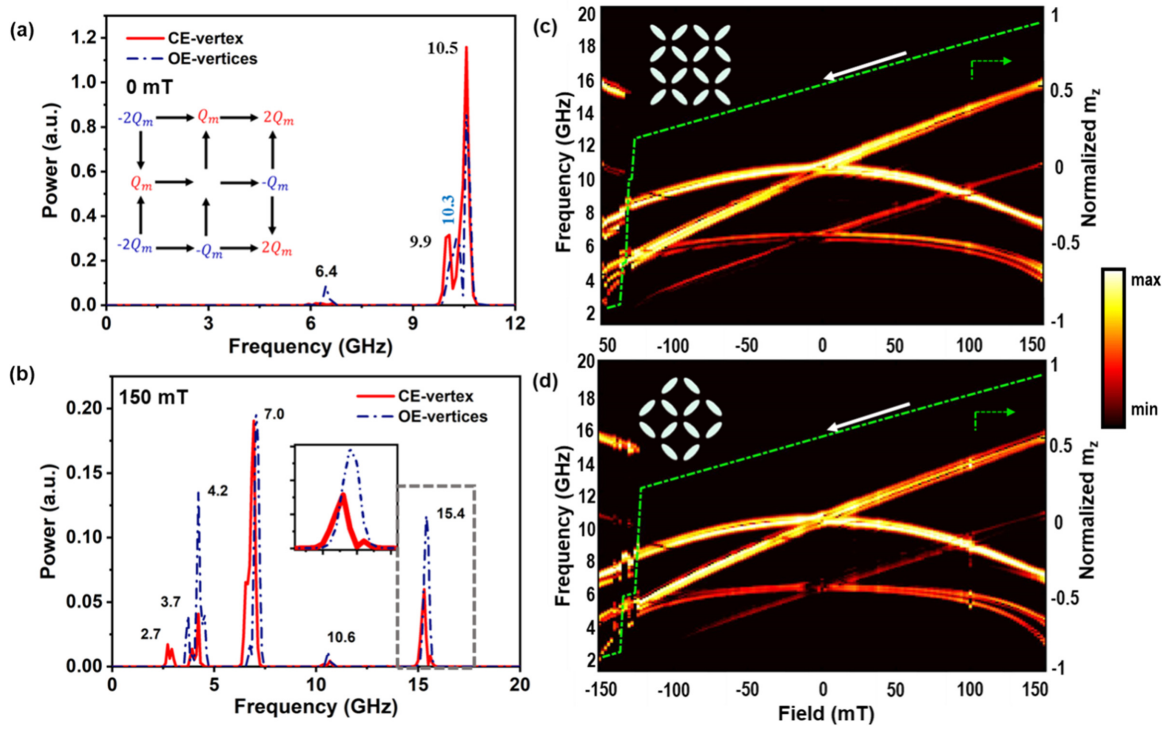

FIG. 8. SW spectra for CE and OE vertices at remanence, i.e., $\vec{B}_{\text{ext}} = 0$ mT (a) and at $\vec{B}_{\text{ext}} = 150$ mT (b) applied along one of the easy axes. The schematic of macrospins arrangement and uncompensated charges at odd coordination vertices for CE vertex at remanence is shown as an inset in (a). Zoomed image of the peak appearing at 15.4 GHz (highlighted in black dash box) at $\vec{B}_{\text{ext}} = 150$ mT is shown as an inset in (b). (c) Dependence of SW modes' frequency on bias field applied along one of the easy axes (left ordinate) as a 2D surface plot and normalized magnetization vs. bias field strength (right ordinate) plot during down-sweep for OE-vertices and (d) CE-vertex. The power of the SW mode is shown in dB to visualize the weaker modes in contrast to strong modes clearly. The intensity of the power is displayed in the colorbar on the right. The white arrow indicates the direction of the bias field sweep (down-sweep). For clarity, schematics of OE and CE vertices are provided as insets in their respective 2D-surface plots (c, d).

show the spectra for nonpolaronic charge cloud state which exhibits only two modes at 9.9 and 10.5 GHz, respectively. The observed slight shift in SW modes in polaron I and polaron II is most likely due to the different charge distribution at the even- and odd-coordinated vertices resulting in a different distribution of the dipolar field. Interestingly, we observe that for a sASI system comprising of completely uncharged vertices, only a single bulk mode at 10.4 GHz is excited [see Figs. 2(d), 3(b), and 6(c)]. The presence of magnetic charges at the center of vertices or a charge cloud (Fig. 7)leads to an additional bulk mode. However, for a monopole polaronic state in the sASI system, we observe a further additional bulk mode, i.e., three bulk modes altogether. The profiles of the peaks in the SW spectra for the two monopole polaronic cases suggest that the SW spectra may be used to determine the monopole polaronic state in such systems. Thus, our results may suggest that the presence of monopole-polaron in such structures lifts the degeneracy of the fundamental bulk modes.

As it is now clear that the SW excitation and their limited propagational behavior in these systems depend on the exact magnetic microstate where dipolar interaction plays a significant role, we next investigate the evolution of SW spectra in the varying field for both CE and OE vertices. The investigation is carried out in the field range of ±150 mT since in this range underlying magnetization is in a nonsaturated state. Therefore, the role of dipolar interactions is significant in stabilizing the magnetic state of the vertex systems. For comparison, the resulting SW spectra for the two types of vertices at varying fields are shown in Fig. 8. Figures 8(c) and 8(d) represent the evolution of SW modes (excitation frequencies) as a function of static bias field applied along one of the easy axes of sASI. The simulations were carried out at every 2-mT field in the entire field range of ±150 mT. Initially at 150 mT, both CE and OE vertices display two strong modes at ∼7.0 GHz and 15.4 GHz and three weak modes are also tabulated in Table I. To clearly visualize the weak modes having relatively low intensity, the power of the modes in the entire field range is displayed in dB as a 2D surface plot. Interestingly, we observe that for CE vertex, all the modes (at all fields) are split into two modes, whereas for OE vertex, *only the B mode is split* in the presence of charged vertex at remanence [Fig. 8(a)]. A representative spectrum showing splitting of all modes of CE vertex and unsplit modes of OE vertex at 150 mT

TABLE I. The Eigen frequencies of SW modes excited in OE and CE vertex at an external magnetic field of 150 mT.

sASI vertex type	Frequency of SW modes (GHz)
OE	∼3.7, 4.2, 7.0, 10.6, 15.4
CE	∼2.7, 4.2, 6.9, 10.6, 15.3

is shown in Fig. 8(b). At this field, the CE vertex does not exhibit any magnetic charge. The split modes suggest that the oscillations occur at slightly different frequencies in different nanomagnets. Our careful investigation of power profiles (see Fig. S5 in the Supplemental Material [49]) indeed shows that the magnetization of nanomagnets at the edges and the inner positions oscillate separately at slightly different frequencies resulting in the split modes. Further, we focus on the behavior of two prominent SW modes appearing at 15.5 and 7 GHz at $\vec{B}_{\text{ext}} = 150$ mT. As shown in Fig. 8, the 15.5-GHz mode, which is the fundamental bulk mode associated with E islands, shows a linear response from 150 mT to a negative bias field of -128 and -122 mT for OE and CE vertices, respectively. The 7-GHz mode is the fundamental bulk mode associated with H islands which shows a nonlinear behavior for both OE and CE vertices. We find that except for mode splitting, all the modes for OE and CE vertices show similar behavior in the presence of a field. A mode jump is observed at -128 mT (OE vertex) and -122 mT (CE vertex), which is due to the increase in the effective field as a result of the sharp switching of magnetization in nanomagnets. The magnetization behavior is shown by dashed-dotted green lines in Figs. 8(c) and 8(d). Before the switching occurs, E islands are subjected to decreasing effective field during down-sweep of external bias field with underlying magnetization configuration remaining effectively the same. Therefore, the frequency of fundamental SW mode due to uniform spin alignment follows a linear trend in accordance with Larmour precession $f \propto H_{\text{eff}}$ down to the switching field. On the other hand, the bulk mode associated with H islands behaves differently as internal spins rotate to align themselves along the easy axis as the field is swept from 150 to 0 mT. This results in symmetric nonlinear SW dispersion with respect to zero bias field. In summary, from our detailed studies of finite-size sASI system, we find excitation of edge and bulk modes due to the local application of pulse field at the central vertex. While the edge mode appears localized, the bulk mode excited at the central vertex exhibits limited propagation to only 4NN with reduced intensity. The bulk mode also exhibits splitting in the presence of *individual* charged vertices (emergent monopole or antimonopole) due to oscillations in two different nanomagnets at the two nearby frequencies. Our observations suggest that the direction of "propagation" in the unconnected nanomagnets is affected by the presence of magnetic charges at the vertices. The distinct signature of three split SW modes is observed as the charge at the central vertex is screened by the charge cloud at the border, forming a magnetic monopole polaron. A comparison of SW modes for CE and OE vertices shows that except splitting of SW modes for the CE vertex case, there is no significant difference in the behavior of modes. The modes are found to be highly tunable in the presence of an external bias field and are considered as potential candidates for magnonic crystals. Our studies show that spectral signatures can be used to identify charged vertices as well as a monopole polaronic state.

ACKNOWLEDGMENTS

We acknowledge the High-Performance Computation (HPC) facility of IIT Delhi. N.A. is thankful to the Council of Scientific Industrial Research (CSIR), Government of India, for the research fellowship.

[1] V. Kruglyak, S. Demokritov, and D. Grundler, Magnonics, J. Phys. D: Appl. Phys. **43**, 260301 (2010).

[2] A. V. Chumak, Magnon spintronics: Fundamentals of magnon-based computing, in *Spintronics Handbook: Spin Transport and Magnetism, Second Edition* (CRC Press, Boca Raton, FL, 2019), pp. 247–302.

[3] Y. Au, M. Dvornik, O. Dmytriiev, and V. Kruglyak, Nanoscale spin wave valve and phase shifter, Appl. Phys. Lett. **100**, 172408 (2012).

[4] M. A. Abeed and S. Bandyopadhyay, Experimental demonstration of an extreme subwavelength nanomagnetic acoustic antenna actuated by spin-orbit torque from a heavy metal nanostrip, Adv. Mater. Technol. **5**, 1901076 (2020).

[5] Q. Wang, P. Pirro, R. Verba, A. Slavin, B. Hillebrands, and A. V. Chumak, Reconfigurable nanoscale spin-wave directional coupler, Sci. Adv. **4**, e1701517 (2018).

[6] K. Vogt, F. Y. Fradin, J. E. Pearson, T. Sebastian, S. D. Bader, B. Hillebrands, A. Hoffmann, and H. Schultheiss, Realization of a spin-wave multiplexer, Nat. Commun. **5**, 3727 (2014).

[7] M. Kostylev, A. Serga, T. Schneider, B. Leven, and, B. Hillebrands, Spin-wave logical gates, Appl. Phys. Lett. **87**, 153501 (2005).

[8] A. Papp, W. Porod, A. I. Csurgay, and G. Csaba, Nanoscale spectrum analyzer based on spin-wave interference, Sci. Rep. **7**, 9245 (2017).

[9] J. Chen, H. Wang, T. Hula, C. Liu, S. Liu, T. Liu, H. Jia, Q. Song, C. Guo, Y. Zhang *et al.*, Reconfigurable spinwave interferometer at the nanoscale, Nano Lett. **21**, 6237 (2021).

[10] H. Yu, G. Duerr, R. Huber, M. Bahr, T. Schwarze, F. Brandl, and D. Grundler, Omnidirectional spin-wave nanograting coupler, Nat. Commun. **4**, 2702 (2013).

[11] J. Grollier, D. Querlioz, and M. D. Stiles, Spintronic nanodevices for bioinspired computing, Proc. IEEE **104**, 2024 (2016).

[12] H. Arava, P. M. Derlet, J. Vijayakumar, J. Cui, N. S. Bingham, A. Kleibert, and L. J. Heyderman, Computational logic with square rings of nanomagnets, Nanotechnology **29**, 265205 (2018).

[13] H. Arava, N. Leo, D. Schildknecht, J. Cui, J. Vijayakumar, P. M. Derlet, A. Kleibert, and L. J. Heyderman, Engineering Relaxation Pathways in Building Blocks of Artificial Spin Ice for Computation, Phys. Rev. Appl. **11**, 054086 (2019).

[14] J. Torrejon, M. Riou, F. A. Araujo, S. Tsunegi, G. Khalsa, D. Querlioz, P. Bortolotti, V. Cros, K. Yakushiji, A. Fukushima *et al.*, Neuromorphic computing with nanoscale spintronic oscillators, Nature (London) **547**, 428 (2017).

[15] F. Caravelli, G.-W. Chern, and C. Nisoli, Artificial spin ice phase-change memory resistors, New J. Phys. **24**, 023020 (2022).

[16] Y. Li, T. Polakovic, Y. L. Wang, J. Xu, S. Lendinez, Z. Zhang, J. Ding, T. Khaire, H. Saglam, R. Divan *et al.*, Strong

Coupling between Magnons and Microwave Photons in On-Chip Ferromagnet-Superconductor Thin-Film Devices, Phys. Rev. Lett. **123**, 107701 (2019).

[17] S. Neusser and D. Grundler, Magnonics: Spin waves on the nanoscale, Adv. Mater. **21**, 2927 (2009).

[18] S. O. Demokritov and A. N. Slavin, *Magnonics: From Fundamentals to Applications*, Vol. 125 (Springer, New York, 2012).

[19] S. A. Nikitov, D. V. Kalyabin, I. V. Lisenkov, A. N. Slavin, Y. N. Barabanenkov, S. A. Osokin, A. V. Sadovnikov, E. N. Beginin, M. A. Morozova, Y. P. Sharaevsky *et al.*, Magnonics: A new research area in spintronics and spin wave electronics, Phys. Usp. **58**, 1002 (2015).

[20] R. Wang, C. Nisoli, R. S. d. Freitas, J. Li, W. McConville, B. Cooley, M. Lund, N. Samarth, C. Leighton, V. H. Crespi *et al.*, Artificial 'spin ice' in a geometrically frustrated lattice of nanoscale ferromagnetic islands, Nature (London) **439**, 303 (2006).

[21] J. Sklenar, V. Bhat, L. DeLong, and J. Ketterson, Broadband ferromagnetic resonance studies on an artificial square spin-ice island array, J. Appl. Phys. **113**, 17B530 (2013).

[22] M. Jungfleisch, W. Zhang, E. Iacocca, J. Sklenar, J. Ding, W. Jiang, S. Zhang, J. E. Pearson, V. Novosad, J. B. Ketterson, O. Heinonen, and A. Hoffmann, Dynamic response of an artificial square spin ice, Phys. Rev. B **93**, 100401(R) (2016).

[23] E. Iacocca, S. Gliga, R. L. Stamps, and O. Heinonen, Reconfigurable wave band structure of an artificial square ice, Phys. Rev. B **93**, 134420 (2016).

[24] D. M. Arroo, J. C. Gartside, and W. R. Branford, Sculpting the spin-wave response of artificial spin ice via microstate selection, Phys. Rev. B **100**, 214425 (2019).

[25] A. Talapatra, N. Singh, and A. Adeyeye, Magnetic Tunability of Permalloy Artificial Spin Ice Structures, Phys. Rev. Appl. **13**, 014034 (2020).

[26] E. Iacocca, S. Gliga, and O. G. Heinonen, Tailoring Spin-Wave Channels in a Reconfigurable Artificial Spin Ice, Phys. Rev. Appl. **13**, 044047 (2020).

[27] S. Gliga, E. Iacocca, and O. G. Heinonen, Dynamics of reconfigurable artificial spin ice: Toward magnonic functional materials, APL Mater. **8**, 040911 (2020).

[28] J. C. Gartside, A. Vanstone, T. Dion, K. D. Stenning, D. M. Arroo, H. Kurebayashi, and W. R. Branford, Reconfigurable magnonic mode-hybridisation and spectral control in a bicomponent artificial spin ice, Nat. Commun. **12**, 2488 (2021).

[29] M. T. Kaffash, S. Lendinez, and M. B. Jungfleisch, Nanomagnonics with artificial spin ice, Phys. Lett. A **402**, 127364 (2021).

[30] W. Bang, M. Kaffash, M. Hossain, A. Hoffmann, J. Ketterson, and M. Jungfleisch, Spin dynamics in permalloy nano-ellipses for honeycomb and square lattices, AIP Adv. **12**, 035131 (2022).

[31] A. K. Chaurasiya, A. K. Mondal, J. C. Gartside, K. D. Stenning, A. Vanstone, S. Barman, W. R. Branford, and A. Barman, Comparison of spin-wave modes in connected and disconnected artificial spin ice nanostructures using brillouin light scattering spectroscopy, ACS Nano **15**, 11734 (2021).

[32] M. B. Jungfleisch, J. Sklenar, J. Ding, J. Park, J. E. Pearson, V. Novosad, P. Schiffer, and A. Hoffmann, High Frequency Dynamics Modulated by Collective Magnetization Reversal in Artificial Spin Ice, Phys. Rev. Appl. **8**, 064026 (2017).

[33] Y. Li, G. Gubbiotti, F. Casoli, S. A. Morley, F. J. Goncalves, M. C. Rosamond, E. H. Linfield, C. H. Marrows, S. McVitie, and R. Stamps, Thickness dependence of spin wave excitations in an artificial square spin ice-like geometry, J. Appl. Phys. **121**, 103903 (2017).

[34] S. Lendinez, M. T. Kaffash, and M. B. Jungfleisch, Emergent spin dynamics enabled by lattice interactions in a bicomponent artificial spin ice, Nano Lett. **21**, 1921 (2021).

[35] F. Montoncello, L. Giovannini, W. Bang, J. Ketterson, M. Jungfleisch, A. Hoffmann, B. W. Farmer, and L. E. De Long, Mutual influence between macrospin reversal order and spin-wave dynamics in isolated artificial spin ice vertices, Phys. Rev. B **97**, 014421 (2018).

[36] N. Arora and P. Das, Spin wave spectral probing of degenerate microstates in building-block of square artificial spin ice, AIP Adv. **11**, 035030 (2021).

[37] S. Lendinez, M. Taghipour Kaffash, and M. B. Jungfleisch, Observation of mode splitting in artificial spin ice: A comparative ferromagnetic resonance and brillouin light scattering study, Appl. Phys. Lett. **118**, 162407 (2021).

[38] S. Gliga, A. K. akay, R. Hertel, and O. G. Heinone, Spectral Analysis of Topological Defects in an Artificial Spin-Ice Lattice, Phys. Rev. Lett. **110**, 117205 (2013).

[39] S. Kempinger, Y.-S. Huang, P. Lammert, M. Vogel, A. Hoffmann, V. H. Crespi, P. Schiffer, and N. Samarth, Field-Tunable Interactions and Frustration in Underlayer-Mediated Artificial Spin Ice, Phys. Rev. Lett. **127**, 117203 (2021).

[40] J. C. Gartside, K. D. Stenning, A. Vanstone, H. H. Holder, D. M. Arroo, T. Dion, F. Caravelli, H. Kurebayashi, and W. R. Branford, Reconfigurable training and reservoir computing in an artificial spin-vortex ice via spin-wave fingerprinting, Nat. Nanotechnol. **17**, 460 (2022).

[41] N. Keswani, R. J. Lopes, Y. Nakajima, R. Singh, N. Chauhan, T. Som, D. S. Kumar, A. R. Pereira, and P. Das, Controlled creation and annihilation of isolated robust emergent magnetic monopole like charged vertices in square artificial spin ice, Sci. Rep. **11**, 13593 (2021).

[42] M. Saccone, K. Hofhuis, Y. L. Huang, S. Dhuey, Z. Chen, A. Scholl, R. V. Chopdekar, S. Van Dijken, and A. Farhan, Dipolar cairo lattice: Geometrical frustration and short-range correlations, Phys. Rev. Mater. **3**, 104402 (2019).

[43] A. Farhan, A. Scholl, C. F. Petersen, L. Anghinolfi, C. Wuth, S. Dhuey, R. V. Chopdekar, P. Mellado, M. J. Alava, and S. Van Dijken, Thermodynamics of emergent magnetic charge screening in artificial spin ice, Nat. Commun. **7**, 12635 (2016).

[44] G.-W. Chern and P. Mellado, Magnetic monopole polarons in artificial spin ices, Europhys. Lett. **114**, 37004 (2016).

[45] I. Gilbert, G.-W. Chern, S. Zhang, L. O'Brien, B. Fore, C. Nisoli, and P. Schiffer, Emergent ice rule and magnetic charge screening from vertex frustration in artificial spin ice, Nat. Phys. **10**, 670 (2014).

[46] A. Vansteenkiste, J. Leliaert, M. Dvornik, M. Helsen, F. Garcia-Sanchez, and B. Van Waeyenberge, The design and verification of mumax3, AIP Adv. **4**, 107133 (2014).

[47] K. H. J. Buschow, *Handbook of Magnetic Materials* (Elsevier, Amsterdam, 2003).

[48] A. Barman and S. Barman, Dynamic dephasing of magnetization precession in arrays of thin magnetic elements, Phys. Rev. B **79**, 144415 (2009).

[49] See Supplemental Material at http://link.aps.org/supplemental/10.1103/PhysRevB.106.184411 for detailed methodology and power profiles information.

[50] C. Castelnovo, R. Moessner, and S. L. Sondhi, Magnetic monopoles in spin ice, Nature (London) **451**, 42 (2008).

[51] N. Keswani, R. Singh, Y. Nakajima, T. Som, and P. Das, Accessing low-energy magnetic microstates in square artificial spin ice vertices of broken symmetry in static magnetic field, Phys. Rev. B **102**, 224436 (2020).